COMMUNICATION

Capacitive Soft Strain Sensors via Multicore–Shell Fiber Printing

Andreas Frutiger, Joseph T. Muth, Daniel M. Vogt, Yiğit Mengüç, Alexandre Campo, Alexander D. Valentine, Conor J. Walsh, and Jennifer A. Lewis*

Recent interest in wearable electronics,[1–8] human/machine interfaces,[9,10] soft exosuits,[11–14] and soft robotics,[15–20] among other areas,[21–29] has motivated an entirely new class of electronic devices – known as stretchable electronics. One embodiment of particular interest is soft sensors that can be textile-mounted.[7,8] Such sensors are composed of a deformable conducting material patterned onto, attached to, or encapsulated within a soft stretchable matrix. To date, multiple sensing mechanisms, fabrication methods, and materials have been employed in these devices.[7,8] To facilitate textile integration, sewing/attaching onto,[30,31] directly sewing into,[32] and weaving into,[33] fabric have been demonstrated.

Resistive soft sensors are based on a resistance change that occurs when a conductor changes its geometry in response to an applied strain.[34–36] They are typically fabricated by lithography,[4,37–40] planar printing,[41–43] embedded 3D printing,[44] micromolding,[45–47] and coating.[48–52] Conductive features composed of eutectic gallium indium (eGaIn),[53,54] carbon[1,4,22,44] and silver[37,38,43] filled materials, and ionic fluids[55–58] have been successfully demonstrated to date. However, each of these materials choices has limitations. For example, the high surface tension and complex surface phenomenon in liquid metals give rise to more complex fabrication routes.[25] By contrast, carbon inks and ionically conductive solutions are easier to pattern; however, they suffer from hysteresis due to changes in electrical resistivity that arise either from particle network disruption at high strains[27,44] or changes in water content due to evaporation or hygroscopic effects when used in resistive-based sensing motifs.[47,55,56]

To overcome the above limitations, we created textile-mounted, capacitive soft strain sensor (CS3) fibers for detecting elongational strains. To date, capacitive sensors have primarily been used in pressure, tactile, or shear sensing.[49,51,59–63] Capacitive sensors typically consist of a dielectric layer sandwiched between two conductive layers, whose thickness changes in response to an applied deformation.[58,64–68] We fabricate CS3 fibers via the multicore–shell printing approach described in **Figure 1** (and, also Movie S1, Supporting Information).[69] Each fiber consists of four concentric, alternating layers of an ionically conductive fluid and a silicone elastomer that serve as the conductor and dielectric/encapsulant, respectively. These materials, which are described in further detail below, are coextruded in the desired configuration using a custom-designed printhead composed of four cylindrical nozzles aligned coaxially (Figures 1a–e and S1, Supporting Information). Conductive and elastomeric inks that ultimately form each concentric layer are loaded into separate reservoirs and then coprinted (Figure S2, Supporting Information). The resulting four-layer configuration produces capacitive fibers whose dimensions are dictated by the relative nozzle sizes, respective flow rates of the ink in each layer, and printing speed. We specifically produced multicore–shell CS3 fibers of various lengths with core diameter of 335 ± 6 μm, dielectric thickness of 164 ± 10 μm, outer conductor thickness 135 μm, encapsulation layer thickness 277 μm, and overall filament width of 1.5 ± 0.05 mm by prescribing flow rates of 0.251, 0.754, 1.257, and 4.021 μL s^{-1} to each of the layers, respectively, and translating the printhead at 4 mm s^{-1}. At the ends of each sensor, the print speed was decreased to 2 mm s^{-1}, resulting in increased layer thicknesses that enabled attachment of electrical connections. Using our multicore–shell printing approach, CS3s can be created in a flexible, highly programmable manner. The sensor architecture can be customized by varying the respective inner (nested) and outer nozzle sizes, ink flow rates, print speed, and print path length.

To facilitate printing and concentric alignment of these multicore–shell fibers, viscoelastic silicone elastomers are used for the encapsulating and dielectric layers. Specifically, we modified a commercially available silicone, Dragonskin 10, by adding both a thickening agent and curing retarder to tailor its rheological properties and extend its pot life (printing window). The modified Dragonskin 10 possesses a yield stress and a sufficiently high shear elastic modulus ($G' \approx 10^3$ Pa) to encapsulate the ionically conductive fluid layers within the concentrically layered fiber architecture (**Figure 2**a). Upon printing and subsequent thermal curing, the high extensibility of Dragonskin 10 (≈1000% strain to failure)[70] allow the fiber sensors to remain intact up to 700% strain (Figures 2b–d). We also developed a nonvolatile, ionically conductive ink composed of glycerol, sodium chloride, and polyethylene glycol ($M_W = 1500$ g mol^{-1}). We note that significant water absorption can occur in the ionically conductive layers due to the high gas permeability of the encapsulating silicone layers and the hygroscopic nature of glycerol.[71] During a one-month period, the weight of an isolated sample of conductive fluid increased by 30%, leading to a concomitant increase in ink conductivity from 50 μS cm^{-1} to 3 mS cm^{-1}. Although such pronounced fluctuations in conductivity will affect the resistance and decay time of our CS3 fibers; we show that when used in a capacitive motif, sensor

A. Frutiger, D. M. Vogt, Prof. Y. Mengüç, Prof. A. Campo, Prof. C. J. Walsh
60 Oxford Street, Cambridge, MA 02138, USA
E-mail: walsh@seas.harvard.edu
J. T. Muth, A. Valentine, Prof. J. A. Lewis
Pierce Hall Rm 221
29 Oxford Street, Cambridge, MA 02138, USA
E-mail: jalewis@seas.harvard.edu
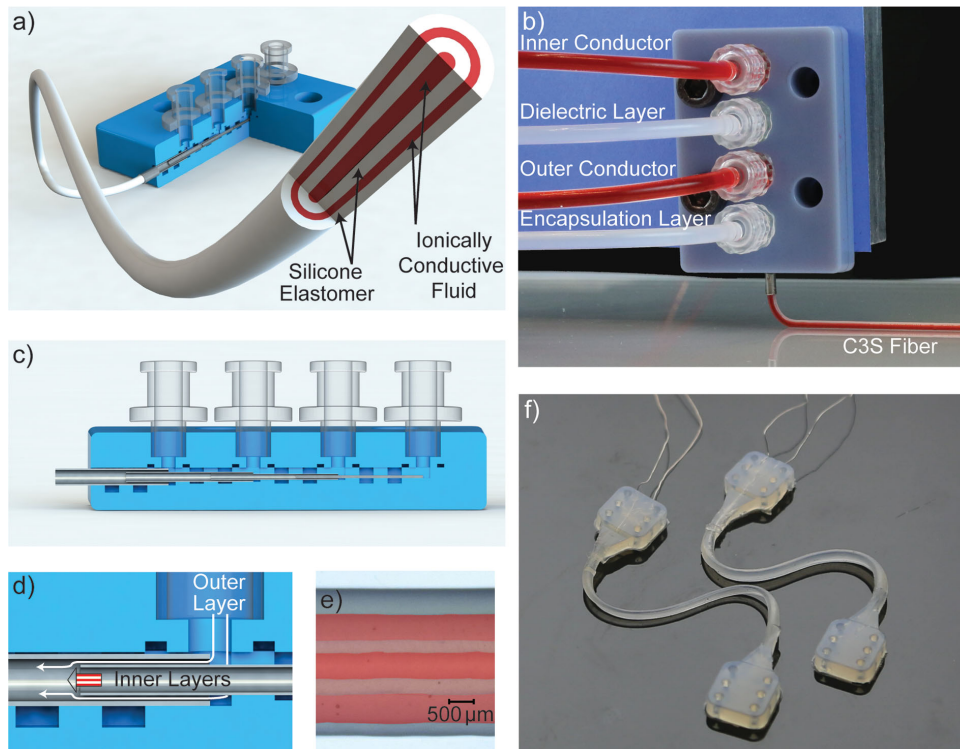
Figure 1. a) Schematic illustration and b) image of multicore-shell printing process. c,d) Schematic illustrations of the printhead design and higher magnification view of the outlet region. e) Optical image of a printed multicore–shell sensor filament with dyed solutions. f) Two CS3s of different lengths.

output is insensitive to conductivity changes (see derivation in the Supporting Information). However, the volumetric expansion associated with water uptake may affect sensor output (Figure S3, Supporting Information). Over the same time period, the conductive ink stiffness decreases by three orders of magnitude (Figure 2a). This does not adversely affect sensor
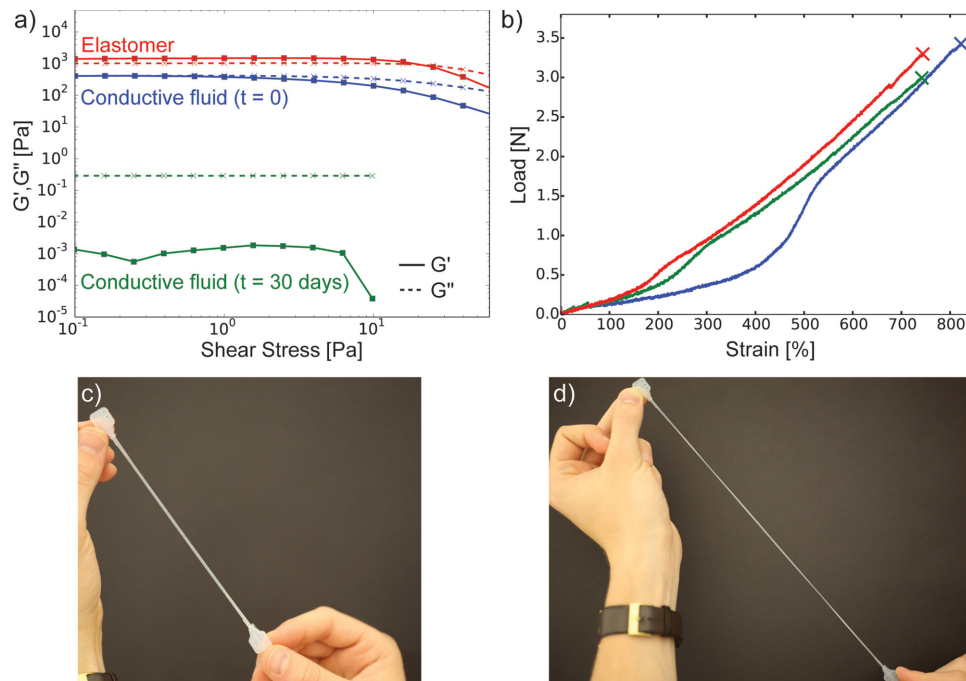
Figure 2. a) Shear elastic and loss moduli as a function of shear stress for the elastomeric dielectric/encapsulant and ionically conductive fluid inks. b) Representative maximum elongation data for three CS3s. c,d) Sensors strained to 0% and ≈150% strain, respectively.
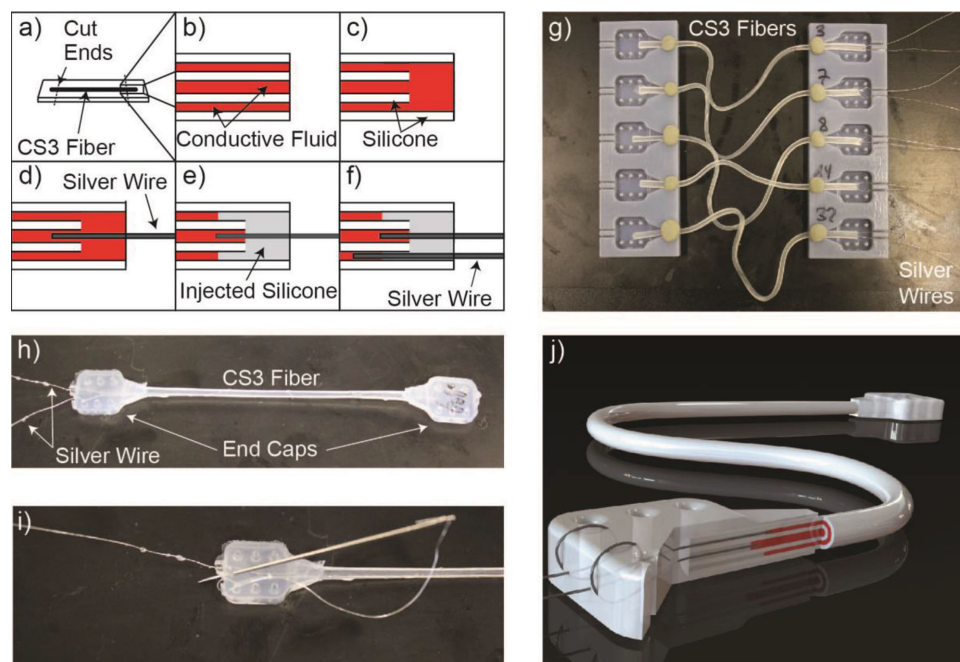
Figure 3. a–f) Schematic illustration of sensor assembly process. g) End cap molding of printed sensors. h) Molded sensor with embedded silver wires for electrical connection. i) Sewing silver wires within rigid elastomer end caps. j) Schematic view of the completed sensor showing the electrical connection and end cap.

performance, since the ionically conductive fluid layers do not significantly contribute to load transmission and are surrounded by silicone

To establish an electrical connection to the CS3 fibers, silver wires (diameter = 127 μm) are embedded into each of the conductive layers after printing and curing. The connection process is illustrated in **Figure 3**a–f and Movie S2, Supporting Information. First, the CS3 fiber tips are trimmed to expose the inner layers of the filament. A few millimeters of the inner silicone tube are pulled out of the fiber and cut (Figure 3c). Subsequently, a silver wire is placed within the inner core (Figure 3d) and isolated by displacing the ionic fluid by injecting a higher shore hardness silicone (Dragonskin 30), which provides a smoother transition between the soft sensor and the rigid wires (Figure 3e). Upon curing the stiffer silicone, a second wire is then inserted into the outer conductive layer (Figure 3f). Silicone endcaps (Dragonskin 30), containing through holes for the wires, are then molded and anchored to the sensor assembly to improve device robustness and facilitate textile integration (Figure 3g). Finally, the wires are sewn through the end caps to inhibit connection pullout (Figure 3h,i). Two representative sensors are shown in Figure 1d, while a schematic view of the completed sensor with a cutaway showing the electrical connection is shown in Figure 3j.

To model sensor response, a lumped element model is applied to a unit cross-section of the sensor (**Figure 4**a). The sensor can be analyzed in terms of three components – a cylindrical resistor (R_i), a cylindrical capacitor (C_s), and a cylindrical ring resistor (R_o) – arranged in series. When an axial strain (ε) is applied to the geometry, the sensor capacitance (C_s), resistance (R_s), and decay time (τ_s) vary linearly, quadratically, and cubically with elongation (derivation and readout electronics

are described in the Supporting Information), respectively, as given by Equations (1)–(3).

$$C_s(\varepsilon) = \frac{2\pi\epsilon\epsilon_0}{\ln\left(\frac{r_{20}}{r_{10}}\right)}(\varepsilon+1)L_0 \tag{1}$$

$$R_s(\varepsilon) = \rho\frac{(\varepsilon+1)^2\frac{L_0}{2}}{\pi}\left(\frac{1}{r_{30}^2 - r_{20}^2} + \frac{1}{r_{10}^2}\right) \tag{2}$$

$$\begin{aligned}\tau(\varepsilon) &= C_{s0}R_{s0}\varepsilon^3 + (C_pR_{s0} + 3C_{s0}R_{s0})\varepsilon^2 \\ &\quad + (2C_pR_{s0} + C_{s0}R_m + 3C_{s0}R_{s0})\varepsilon + C_pR_m \\ &\quad + C_pR_{s0} + C_{s0}R_m + C_{s0}R_{s0}\end{aligned} \tag{3}$$

where ϵ is the dielectric permittivity of the ionically conductive fluid, ϵ_0 is the dielectric permittivity of vacuum, L_0 is the initial length of the sensor, ρ is the resistivity of the ionic fluid, C_{s0} is the zero strain capacitance of the sensor, R_{s0} is the zero strain resistance of the sensor, C_p is the parasitic capacitance of the system, R_m is the resistance of the measurement resistor in the readout electronics, and r_{10}, r_{20}, and r_{30} are the outer radii of the ionic fluid core, dielectric layer, and ionic fluid shell, respectively.

We first measured their static response by elongating and retracting six sensors a total of three times. One hundred measurements of capacitance, resistance, and decay time are acquired per data point and averaged. Figure 4b,c show representative capacitance, resistance and decay time responses as a function of strain. Resistance and capacitance measurements
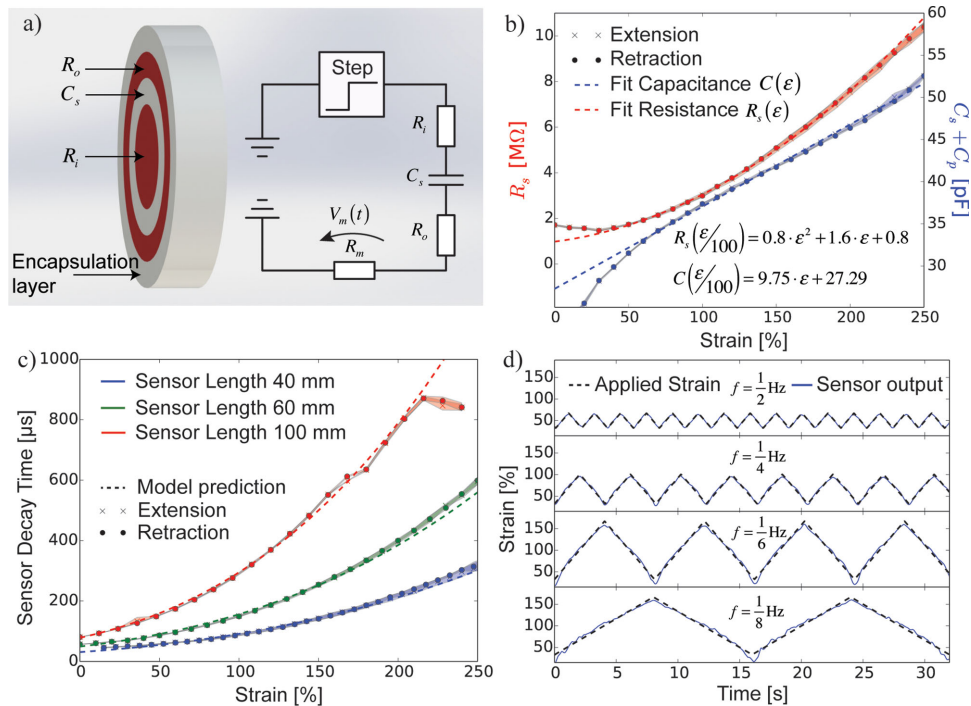
Figure 4. a) Sensor cross-section with lumped element properties and equivalent circuit diagram of the readout circuitry. b) Model predictions, sensor resistance, and total capacitance of the sensor up to 250% strain. c) Model predictions and decay time data for three sensors of different length up to 250% strain. d) Dynamic sensor capacitance output after normalization and filtering for different strain amplitudes and frequencies.

are shown for a 60 mm sensor, while the decay time response is displayed for sensors of length 40, 60, and 100 mm. The shaded areas in the plots represent the maximum and minimum averaged values encountered in the three cycles. Sensor outputs are collected by analyzing the voltage decay across the measurement resistor after a step voltage is applied to the system (see readout electronics, Supporting Information). The model for each sensing quantity agreed well with the experimentally observed responses up to 250% strain. Above 250% strain, the sensor resistance becomes too large (> 10 MΩ) to be accurately captured by the current readout electronics. If their resistance remained below 10 MΩ throughout testing, the sensors would remain functional over the entire extensibility range (i.e., ≈700% strain). At low strains, their observed deviation from model predictions most likely stems from inadequate tension in the dielectric layer to ensure a straight inner tube. Prestraining the sensor may eliminate discrepancies between the predicted and experimentally observed sensor performance at these strain levels. Fitting the resistance and capacitance data to the sensor model (Equations (S8) and (S9), Supporting Information) allowed the sensor capacitance, parasitic capacitance, and sensor resistance (sensor performance, Table S1, Supporting Information) to be determined. For a 60 mm sensor, we measure a sensor capacitance of 9.75 pF, parasitic capacitance of 17.54 pF, and a sensor resistance of 0.8 MΩ. Sensitivity corresponds to the sensors' capacitance and amounted to 9.75 pF change per 100% strain for the 60 mm sensor. The gauge factor for the capacitive response of the sensors is 0.348 ± 0.11. In principle, the sensor can output any of these three quantities: capacitance, resistance, and decay time. As shown in Figure S4, Supporting Information, the signal-to-noise ratio of resistance

and decay time measurements is higher compared to the corresponding capacitance value. However, resistance and decay time measurements produce nonlinear outputs with strain (Equations (2) and (3)) and are susceptible to environmental conditions that give rise to conductivity changes. Accurate sensing in the resistive and decay time regimes is possible by measuring the conductivity of the ionically conductive fluid in an unstretched reference reservoir exposed to the same environmental conditions as a calibration standard.

Our results indicate that the sensing characteristics of these CS3 fibers can be tuned by varying their geometry. Figure 4c illustrates predictable changes in decay time as a function of sensor length. Specifically, we compare the sensor output with the model equation for the decay time (Equation (3)), with the necessary parameters (C_{s0}, C_p, and R_{s0}) determined from the capacitance and resistance data. The decay time increases with sensor length due to an increase in sensor resistance and capacitance. We note that alternate nozzle designs and print parameters may be used to vary the relative thicknesses of each layer of the fiber, enabling customized sensor properties. Figure S5, Supporting Information, illustrates predicted changes in capacitive sensitivity as a function of sensor length and relative layer thickness.

We then quantified the dynamic sensor response over a range of applied strain frequencies and amplitudes. Sensor output is filtered with a second order butterworth lowpass filter with a cutoff frequency of 2 Hz. Figure 4d shows the sensor tracks the applied strain input accurately. The unfiltered data, and the corresponding resistance and decay time output, are shown in Figure S4, Supporting Information. The mean averaged error (MAE) of the sensor was <11.5% in the unfiltered state for all

frequencies and amplitudes tested. MAE was reduced to <5% after filter application. MAE is described by Equation (4):

$$\text{MAE} = \frac{1}{n}\sum_{i=1}^{n}\left|y_s\left(\varepsilon\right)-\varepsilon\right| \tag{4}$$

where $y_s(\varepsilon)$ is the strain measured by the sensor, ε is the applied strain, and n is the number of data points sampled. The bandwidth of the sensor combined with the readout electronics is 50–150 Hz. However, the bandwidth of the sensor alone is determined solely by decay time. Hence, for decay times of 200–900 µs at 250% strain (Figure 4c), the possible bandwidth is 500–2500 Hz. For lower strains, higher bandwidths are possible.

To demonstrate the utility of the multicore–shell fibers as a wearable sensor, we mounted them onto textiles by either sewing or weaving (**Figure 5**a–c, respectively) and tested their capacity to capture the gate cycle of a wearer in real time (Figure 5d and Movie S3, Supporting Information). The normalized change in decay time is plotted as a function of time for walking speeds up to 4 mph. The high signal-to-noise ratio of the decay time output enabled both the primary and secondary walking gait peaks to be detected.[72] We note that the capacitive response of the sensor during walking is quite noisy,

which prevents accurate data capture due to limitations associated with the current read-out electronics.

In summary, we report a new method for creating CS3s based on multicore–shell fiber printing. By developing a nonvolatile ionic fluid, modifying a soft silicone elastomer, and arranging them coaxially in a cylindrical capacitor motif, we have created soft sensors with accurate and hysteresis-free performance in both static and dynamic operating conditions. These customizable sensors can be readily integrated with textiles and may find specific application in wearable electronics, human/machine interfaces, soft exosuits, and soft robotics.

Experimental Section

Materials System: The ionic conductive ink is prepared by dissolving as-received sodium chloride until saturation (MACRON) in glycerol (99.5%, Aldrich) under continuous stirring at 100 °C overnight. The glycerol solution is mixed with polyethylene glycol (PEG) (PEG 1500, Aldrich) in a ratio of 10:1 by weight and heated to 100 °C under continuous stirring until all PEG is dissolved. The solution is degassed for 5 min under vacuum and subsequently poured into a plastic 10 mL Becton Dickinson syringe and cooled down to room temperature. The dielectric and encapsulation layer is fabricated from Dragonskin 10 Slow Cure Part A (60 g) and B (60 g), Thi-Vex Silicone Thickener (0.12 g) and Slo-Jo Platinum Silicone Cure Retarder (0.6 g) all obtained from Smooth-On, Inc. Thi-vex modified the rheological properties and the silicone cure retarder increased pot life. Before homogenizing, the solution is degassed under vacuum for 2 min. Homogenizing and additional degassing are performed for 30 s each using a planetary mixer (ARE-310, Thinky Mixer USA) at 2000 and 2200 rpm, respectively. To transfer the final ink into a 5 mL syringe without introducing air, the hole at the tip of a 60 mL syringe is increased to ≈1 cm by using a rotary cutting tool. The ink is then drawn up into the modified syringe and injected into a 5 mL syringe for dispensing with the syringe pumps.

Rheological Characterization: The rheological properties of the conductive ink and the dielectric/encapsulant are characterized under ambient conditions using a controlled stress rheometer (Discovery HR-3 Rheometer, TA Instruments). The rheology of the conductive ink is assessed one day after ink fabrication, while the dielectric/encapsulant is measured immediately after homogenization. The properties of the conductive ink and the dielectric/encapsulant are measured using a 40 mm tapered cone (2.005° taper, 56 µm truncation gap). The conductive ink is also evaluated after aging for 30 days at ambient conditions. For these measurements, a 60 mm cone and plate geometry is utilized (2.000° taper, 55 µm truncation gap). All oscillatory measurements are performed at 21 °C with an angular frequency of 6.28 rad s^{-1} within the strain range of 10^{-4}%–10^{3}%.

Ink Conductivity: Ink conductivity is measured using a bench top conductivity meter (Sper Scientific). Ten ml of ink is allowed to equilibrate for 24 h before a measurement is taken. To evaluate the effect of water absorption on conductivity and rheology, 25 petri dishes of size 5.5 mm × 1.2 mm each with 10 g of conductive ink are exposed to ambient conditions. Conductivity (1 sample per measurement) and weight (10 samples per measurement) are measured every 2–4 days for 30 days while oscillatory strain experiments were performed one day and 30 days after ink synthesis. For water absorption of the filaments, six CS3 fibers are weighed after printing and their weight gain is monitored over four days.

Printhead Fabrication: The mount for the printhead is fabricated using a Connex500 3D printer with VeroBlue RGD840 as the feed material. Tubes used to create the nozzle are obtained from McMaster-Carr (Precision Miniature 304 Stainless Steel Tubing) and cut to the corresponding length with a rotary cutting tool. The tube sizes and length are as follows: (Gauge, Inner diameter [mm], Outer diameter [mm], Length [mm]): Core (27,0.254, 0.406,16), Intermediate layer
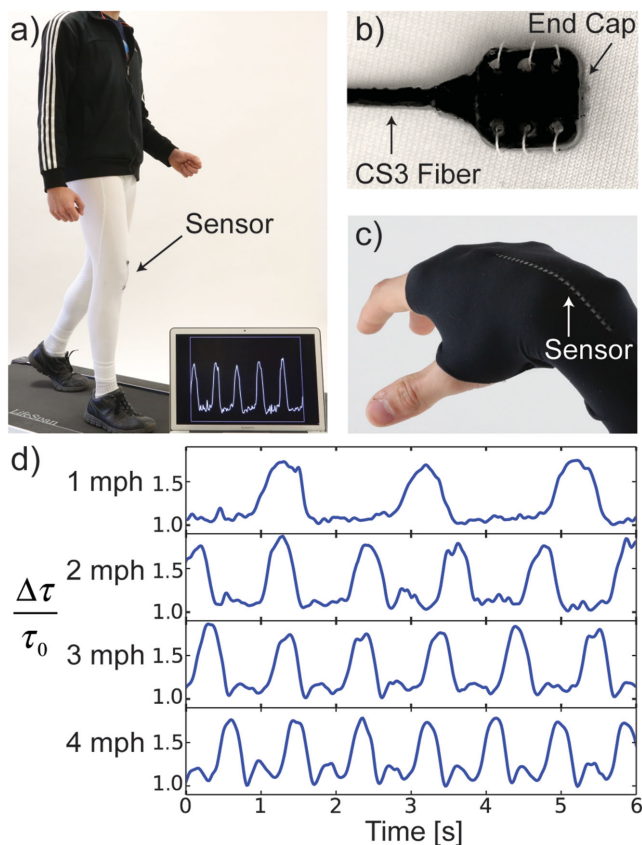
Figure 5. a) Textile-mounted CS3 attached to fabric across the knee. b) Sensor integration with textiles via sewing b) and weaving c). d) Normalized decay time output of the sensor for different walking speeds up to 4 mph.

1 (IL1) (23, 0.431, 0.635, 42), Shell 1 (20.5, 0.685, 0.863, 16), IL2 (19, 0.889, 1.066, 30), Shell 3 (17.5, 1.168, 1.4224, 16) IL3 (15, 1.524, 1.8288, 18), and Shell 4 (13, 1.956, 2.413, 16). The tubes are fixed in place with epoxy (Loctite 5 min Epoxy). A detailed description of the nozzle fabrication is provided in Figure S1, Supporting Information.

Multicore–Shell Printing: Four syringe pumps (two PHD Ultra (Harvard Apparatus – 703007) and two PHD 22/2000 (Harvard Apparatus – 702001)) are used in order to pump the inks through the printhead. The flow rates for each layer are as follows [μL s^{-1}]: Core (0.251), Shell 1 (0.754), Shell 2 (1.257), and Shell 3 (4.021), which should yield the following layer diameters [μm] 364, 610, 879, and 1433. The printhead is attached to a custom built 3D printer (ABG 10000, Aerotech Inc.), which translates the printhead in the prescribed pattern. All print paths are generated using G-code commands. The print height of the nozzle is ≈1 cm above the substrate. Filament thicknesses are assessed for five samples from top-down optical micrographs (VHX 2000, Keyence). Refractive index differences between layers and filament curvature leads to discrepancies between the actual filament dimensions and the imaged dimensions. As such, the reported thickness of the outer conductor and encapsulant are calculated based on the relative flow rates of the material rather than image measurements.

Electrical Connections: For insulating the two conductive layers at the sensor ends, Dragonskin 30 (1 Part A and 1 Part B) are mixed with 0.1 Part Silicone Thinner (Smooth-on, Inc) using a planetary mixer with the same settings as prescribed for Dragonskin 10. After mixing, Dragonskin 30 is injected with a syringe into the filament. The end caps are fabricated by casting Dragonskin 30 (same recipe as above but without any thinner) into 3D printed molds (Connex500, VeroBlue RGD840).

Signal Processing and Readout Electronics: The voltage across a 1 MΩ resistor in series with the sensor is monitored after applying step voltage to the system. From the voltage decay profile, the decay time is calculated. The decay time is then used to obtain both the capacitance and the resistance of the sensor. Data analysis is performed on an ATMEGA328P chip (Arduino Pro Mini, Sparkfun). The step response was 5 V in magnitude and applied at a frequency of 50–200 Hz. The decay voltage is sampled by an internal analog-to-digital converter with a sampling frequency of 75 kHz and 8 bit resolution. Signal segmentation, linearization and sensor quantities are calculated on the device and transmitted via a serial port to a computer. Data acquisition and visualization are performed in Python. A detailed explanation of the data collection algorithm is given in the Supporting Information – Readout Electronics.

Mechanical Testing: The elongation at break is determined by straining the sensors at a crosshead speed of 5 mm s^{-1} until failure (Instron 5544A, Instron).

Static Sensor Testing: We custom designed a testing jig with fixtures that allowed the sensors to be strained to predefined values. The sensors are stretched to the prescribed strain level, attached to the jig, and the relevant outputs were measured. Data are acquired with an ATMEGA328P microcontroller (Sparkfun, Inc.) and transmitted via serial to a computer. For every data point 100 sensor property samples are acquired and averaged. Every sensor is elongated and retracted three times, The shaded areas in Figure 4b,c mark minimun and maximum values measured. The gauge factor is calculated from the static characterization of six sensors.

Dynamic Sensor Testing: The same sensor for which the static characterization is shown was also used for the dynamic testing. The sensor has an original length of 60 mm and for every experiment it was prestrained by 20 mm (33.3% strain) at a velocity of 10 mm s^{-1} and then cycled 20 times at a speed of 20 mm s^{-1} from 80 mm elongation to 100 mm elongation and then again retracted from 80 to 60 mm at a speed of 10 mm s^{-1}. We explored different amplitudes (20, 40, and 80 mm) and for the biggest amplitude also different speeds (10 and 20 mm s^{-1}). This resulted in four different actuation frequencies (1/2, 1/4, 1/6, and 1/8 Hz) and maximum strains of 66.6%, 100%, and 166.66%. Limitations on the maximum crosshead velocity of the load frame (Instron 5544A, Instron) prevented exploration of more rapid

frequencies for the given strain levels. Elongation data are acquired by the Instron, while an ATMEGA328P microcontroller (Sparkfun, Inc.) monitored sensor output.

Walking Tests: The sensor is sewn onto the knee region of spandex athletic tights and the wearer walked at four different speeds on a treadmill (1, 2, 3, and 4 mph). The data are recorded with an average sampling frequency of 65 Hz and processed on an ATMEGA328P microcontroller (Sparkfun, Inc.) and transmitted via serial to a computer, where it was filtered with a low pass filter with a cutoff-frequency of 1.6 Hz.

Supporting Information

Supporting Information is available from the Wiley Online Library or from the author.

[1] T. Yamada, Y. Hayamizu, Y. Yamamoto, Y. Yomogida, A. Izadi-Najafabadi, D. N. Futaba, K. Hata, *Nat. Nanotechnol.* **2011**, *6*, 296.

[2] D. Kim, N. Lu, R. Ma, Y. Kim, R. Kim, S. Wang, J. Wu, S. M. Won, H. Tao, A. Islam, K. J. Yu, T. Kim, R. Chowdhury, M. Ying, L. Xu, M. Li, H. Chung, H. Keum, M. McCormick, P. Liu, Y. Zhang, F. G. Omenetto, Y. Huang, T. Coleman, J. A. Rogers, *Science* **2011**, *333*, 838.

[3] C. Pang, G. Lee, T. Kim, S. M. Kim, H. N. Kim, S. Ahn, K. Suh, *Nat. Mater.* **2012**, *11*, 795.

[4] N. Lu, C. Lu, S. Yang, J. A. Rogers, *Adv. Funct. Mater.* **2012**, *22*, 4044.

[5] D. Kim, Y. Kim, J. Wu, Z. Liu, J. Song, *Adv. Mater.* **2009**, *21*, 3703.

[6] S. Xu, Y. Zhang, L. Jia, K. E. Mathewson, K. Jang, J. Kim, H. Fu, X. Huang, P. Chava, R. Wang, S. Bhole, L. Wang, Y. J. Na, Y. Guan, M. Flavin, Z. Han, Y. Huang, J. A. Rogers, *Science.* **2014**, *344*, 70.

[7] C. Pang, C. Lee, K. Suh, *J. Appl. Polym. Sci.* **2013**, *130*, 1429.

[8] W. Zeng, L. Shu, Q. Li, S. Chen, F. Wang, X. M. Tao, *Adv. Mater.* **2014**, *26*, 5310

[9] H. C. Ko, M. P. Stoykovich, J. Song, V. Malyarchuk, W. M. Choi, C.-J. Yu, J. B. Geddes III, J. Xiao, S. Wang, Y. Huang, J. A. Rogers, *Nature (London)* **2008**, *454*, 748.

[10] D. Kim, R. Ghaffari, N. Lu, J. A. Rogers, *Annu. Rev. Biomed. Eng.* **2012**, *14*, 113.

[11] A. Asbeck, S. De Rossi, K. Holt, C. Walsh, *Int. J. Rob. Res.*, 10.1177/0278364914562476.

[12] A. Asbeck, S. De Rossi, I. Galiana, C. Walsh, *IEEE Rob. Autom. Mag.* **2014**, *21*, 22.

[13] A. Asbeck, K. Schmidt, C. Walsh, *Rob. Auton. Syst.* DOI 10.1016/j.robot.2014.09.025.

[14] Y. Mengüç, Y. L. Park, H. Pei, D. Vogt, P. Aubin, E. Winchell, L. Fluke, L. Stirling, R. J. Wood, C. Walsh, *Int. J. Rob. Res.* **2014**, *33*, 1748.

[15] P. Polygerinos, Z. Wang, K. Galloway, R. J. Wood, C. Walsh, *Rob. Auton. Syst.* DOI 10.1016/j.robot.2014.08.014.

[16] B. Mosadegh, P. Polygerinos, C. Keplinger, S. Wennstedt, R. F. Shepherd, U. Gupta, J. Shim, K. Bertoldi, C. Walsh, G. M. Whitesides, *Adv. Funct. Mater.* **2014**, *24*, 2163.

[17] E. T. Roche, R. Wohlfarth, J. Overvelde, N. Vasilyev, F. Pigula, D. Mooney, K. Bertoldi, C. Walsh, *Adv. Mater.* **2014**, *26*, 1200.

[18] R. V. Martinez, J. L. Branch, C. R. Fish, L. Jin, R. F. Shepherd, R. M. D. Nunes, Z. Suo, G. M. Whitesides, *Adv. Mater.* **2013**, *25*, 205.

[19] R. F. Shepherd, F. Ilievski, W. Choi, S. A. Morin, A. A. Stokes, A. D. Mazzeo, X. Chen, M. Wang, G. M. Whitesides, *Proc. Natl. Acad. Sci. USA* **2011**, *108*, 20400.

[20] J. C. Nawroth, H. Lee, A. W. Feinberg, C. M. Ripplinger, M. L. McCain, A. Grosberg, J. O. Dabiri, K. K. Parker, *Nat. Biotechnol.* **2012**, *30*, 792.

[21] T. Sekitani, T. Someya, *Adv. Mater.* **2010**, *22*, 2228.

[22] T. Sekitani, H. Nakajima, H. Maeda, T. Fukushima, T. Aida, K. Hata, T. Someya, *Nat. Mater.* **2009**, *8*, 494.

[23] C. Keplinger, J. Sun, C. C. Foo, P. Rothemund, G. M. Whitesides, Z. Suo, *Science* **2013**, *341*, 984.

[24] J. So, J. Thelen, A. Qusba, G. J. Hayes, G. Lazzi, M. D. Dickey, *Adv. Funct. Mater.* **2009**, *19*, 3632.

[25] C. Ladd, J. H. So, J. Muth, M. D. Dickey, *Adv. Mater.* **2013**, *25*, 5081.

[26] B. C-K. Tee, C. Wang, R. Allen, Z. Bao, *Nat. Nanotechnol.* **2012**, *7*, 825.

[27] S. Rosset, H. R. Shea, *Appl. Phys. A: Mater. Sci. Process.* **2013**, *110*, 281.

[28] S. Rosset, M. Niklaus, P. Dubois, H. R. Shea, *Adv. Funct. Mater.* **2009**, *19*, 470.

[29] M. L. Hammock, A. Chortos, B. C. K. Tee, J. B. H. Tok, Z. Bao, *Adv. Mater.* **2013**, *25*, 5997.

[30] S. Ma, Y. Wang, Z. Min, L. Zhong, *Polym. Int.* **2013**, *62*, 983.

[31] Y. Menguc, Y.-L. Park, E. Martinez-Villalpando, P. Aubin, M. Zisook, L. Stirling, R. J. Wood, C. Walsh, *2013 IEEE Int. Conf. Rob. Autom.* **2013**, 5289.

[32] C. Mattmann, F. Clemens, G. Tröster, *Sensors* **2008**, *8*, 3719.

[33] M. Sergio, N. Manaresi, M. Tartagni, R. Guerrieri, R. Canegallo, *Proc. IEEE Sens.* **2002**, *2*, 1625.

[34] L. Pan, A. Chortos, G. Yu, Y. Wang, S. Isaacson, R. Allen, Y. Shi, R. Dauskardt, Z. Bao, *Nat. Commun.* **2014**, *5*, 3002.

[35] D. M. Vogt, Y. Park, R. J. Wood, *IEEE Sens. J.* **2013**, *13*, 4056.

[36] Y. Park, B. Chen, R. Wood, *IEEE Sens. J.* **2012**, *12*, 2711.

[37] J. H. Lee, D. Yang, S. Kim, I. Park, *Int. Conf. Solid-State Sens. Actuators Microsyst.* **2013**, *1*, 2624.

[38] X. Z. Niu, S. L. Peng, L. Y. Liu, W. J. Wen, P. Sheng, *Adv. Mater.* **2007**, *19*, 2682.

[39] D.-H. Kim, J. Xiao, J. Song, Y. Huang, J. A. Rogers, *Adv. Mater.* **2010**, *22*, 2108.

[40] D.-H. Kim, J. Song, W. M. Choi, H. Kim, R. Kim, Z. Liu, Y. Y. Huang, K. Hwang, Y. Zhang, J. A. Rogers, *Proc. Natl. Acad. Sci. USA* **2008**, *105*, 18675.

[41] R. Brooke, D. Evans, M. Dienel, P. Hojati-Talemi, P. Murphy, M. Fabretto, *J. Mater. Chem. C* **2013**, *1*, 3353.

[42] C. Lee, L. Jug, E. Meng, *Appl. Phys. Lett.* **2013**, *102*, 183511.

[43] K. Chun, Y. Oh, J. Rho, J. Ahn, Y. Kim, H. R. Choi, S. Baik, *Nat. Nanotechnol.* **2010**, *5*, 853.

[44] J. T. Muth, D. M. Vogt, R. L. Truby, Y. Mengüç, D. B. Kolesky, R. J. Wood, J. A. Lewis, *Adv. Mater.* **2014**, *26*, 6307.

[45] Y. Park, C. Majidi, R. Kramer, P. Bérard, R. J. Wood, *J. Micromech. Microeng.* **2010**, *20*, 125029.

[46] C. Majidi, R. Kramer, R. J. Wood, *Smart Mater. Struct.* **2011**, *20*, 105017.

[47] J. Chossat, Y. Park, R. J. Wood, V. Duchaine, *IEEE Sens. J.* **2013**, *13*, 3405.

[48] F. Xu, Y. Zhu, *Adv. Mater.* **2012**, *24*, 5117.

[49] W. Hu, X. Niu, R. Zhao, Q. Pei, *Appl. Phys. Lett.* **2013**, *102*, 083303.

[50] M. Park, J. Im, M. Shin, Y. Min, J. Park, H. Cho, S. Park, M. Shim, S. Jeon, D. Chung, J. Bae, J. Park, U. Jeong, K. Kim, *Nat. Nanotechnol.* **2012**, *7*, 803.

[51] D. J. Lipomi, M. Vosgueritchian, B. C. K. Tee, S. L. Hellstrom, J. A. Lee, C. H. Fox, Z. Bao, *Nat. Nanotechnol.* **2011**, *6*, 788.

[52] B. S. Shim, W. Chen, C. Doty, C. Xu, N. A. Kotov, *Nano Lett.* **2008**, *8*, 4151.

[53] S. Zhu, J. H. So, R. Mays, S. Desai, W. R. Barnes, B. Pourdeyhimi, M. D. Dickey, *Adv. Funct. Mater.* **2013**, *23*, 2308.

[54] J. W. Boley, E. L. White, G. T. -C. Chiu, R. K. Kramer, *Adv. Funct. Mater.* **2014**, *23*, 3501.

[55] P. Manandhar, P. D. Calvert, J. R. Buck, *IEEE Sens. J.* **2012**, *12*, 2052.

[56] Y.-N. Cheung, Y. Zhu, C.-H. Cheng, C. Chao, W. W.-F. Leung, *Sens. Actuators A* **2008**, *147*, 401.

[57] B. Chen, J. J. Lu, C. H. Yang, J. H. Yang, J. Zhou, Y. M. Chen, Z. Suo, *ACS Appl. Mater. Interfaces* **2014**, *6*, 7840.

[58] J.-Y. Sun, C. Keplinger, G. M. Whitesides, Z. Suo, *Adv. Mater.* **2014**, *26*, 7608.

[59] L. Viry, A. Levi, M. Totaro, A. Mondini, V. Mattoli, B. Mazzolai, L. Beccai, *Adv. Mater.* **2014**, *26*, 2659.

[60] P. Roberts, D. D. Damian, W. Shan, T. Lu, C. Majidi, *2013 IEEE Int. Conf. Rob. Autom.* **2013**, 3514.

[61] C. Metzger, E. Fleisch, J. Meyer, M. Dansachmüller, I. Graz, M. Kaltenbrunner, C. Keplinger, R. Schwödiauer, S. Bauer, *Appl. Phys. Lett.* **2008**, *92*, 013506.

[62] S. C. B. Mannsfeld, B. C.-K. Tee, T. M. Stoltenberg, C. V. H.-H. Chen, S. Barman, B. V. O. Muir, A. N. Sokolov, C. Reese, Z. Bao, *Nat. Mater.* **2010**, *9*, 859.

[63] S. P. Lacour, D. P. J. Cotton, *Int. Conf. Solid-State Sens. Actuators Microsyst.* **2011**, *1*, 2770.

[64] N. A. A. Ridzuan, S. Masuda, N. Miki, *Micro Nano Lett.* **2012**, *7*, 1193.

[65] M. Kollosche, H. Stoyanov, S. Laflamme, G. Kofod, *J. Mater. Chem.* **2011**, *21*, 8292.

[66] D. J. Cohen, D. Mitra, K. Peterson, M. M. Maharbiz, *Nano Lett.* **2012**, *12*, 1821.

[67] D. P. J. Cotton, I. Graz, S. Lacour, *IEEE Sens. J.* **2009**, *9*, 2008.

[68] I. A. Anderson, T. A. Gisby, T. G. McKay, B. M. O'Brien, E. P. Calius, *J. Appl. Phys.* **2012**, *112*, 041101.

[69] D. J. Lorang, D. Tanaka, C. M. Spadaccini, K. A. Rose, N. J. Cherepy, J. A. Lewis, *Adv. Mater.* **2011**, *23*, 5055.

[70] According to the manufacturer's data sheet: Dragonskin 10 Slow, http://www.smooth-on.com/tb/files/DRAGON_SKIN_SERIES_TB.pdf, accessed: January **2015**.

[71] Y. H. Jeong, S. R. Nagel, S. Bhattacharya, *Phys. Rev. A: At. Mol. Opt. Phys.* **1986**, *34*, 602.

[72] M. H. Schwartz, A. Rozumalski, J. P. Trost, *J. Biomech.* **2008**, *41*, 1639.